SYNTHESIS AND APPLICATION OF Ag/CuO/Fe_3O_4/ACB DERIVED FROM *BRUCEA JAVANICA* FOR PHOTOCATALYTIC FENTON DEGRADATION OF CRYSTAL VIOLET DYE

VIET HUNG HOANG[(1)*], VAN THANH NGUYEN[(1)], THI THAO LE[(1)], MINH HIEU DO[(1)], VAN THUAN LE[(2) (3)], VAN DAT DOAN[(4)]

[(1)] *Institute of Tropical Durability, Joint Vietnam - Russia Tropical Science and Technology Research Center*

[(2)] *Center for Advanced Chemistry, Institute of Research & Development, Duy Tan University, Da Nang*

[(3)] *Faculty of Natural Sciences, Duy Tan University, Da Nang*

[(4)] *Faculty of Chemical Engineering, Industrial University of Ho Chi Minh City, Ho Chi Minh City*

**Corresponding author: - Viet Hung Hoang*

- Address: 63 Nguyen Van Huyen, Nghia Do, Hanoi.

- Tel: +84 969323664 Email: hung.hoangviet191290@gmail.com

***- Highlights**:*

- ✓ A multifunctional Ag/CuO/Fe_3O_4/ACB photocatalyst was synthesized via one-step carbonization of *Brucea javanica* seeds, with Ag (~25 nm), CuO (~20 nm), and Fe_3O_4 (~10 nm) nanoparticles uniformly distributed on a porous carbon matrix.
- ✓ Under visible-light heterogeneous heterogeneous photo-Fenton-like-like conditions it delivers 98.0% CV removal in 90 min at pH 7 with 0.05 M H_2O_2 (2 g L^{-1} catalyst) and shows the highest rate among all tested samples (k_1 = 0.0188 min^{-1}).
- ✓ The catalyst is magnetically separable and reusable, retaining ~83% efficiency after five cycles while preserving crystalline and chemical integrity by XRD/FTIR.

- Abstract: The relentless release of organic dyes into water bodies has raised critical environmental concerns, demanding the development of efficient, sustainable, and reusable catalytic systems for wastewater treatment. In this study, we report the synthesis of a multifunctional Ag/CuO/Fe_3O_4/activated carbon beads (ACB) composite derived from natural *Brucea javanica* seeds through a one-step carbonization method. The resulting composite combines the magnetic properties of Fe_3O_4, the visible-light-responsive nature of CuO, and the surface plasmon resonance of Ag, creating a robust catalyst capable of highly efficient heterogeneous heterogeneous photo-Fenton-like-like degradation of crystal violet (CV) dye under visible light. Under optimized conditions (pH 7, H_2O_2 0.05 M, catalyst dosage 2 g/L, and Fe^{3+}:Cu^{2+}:Ag^{+} ratio of 2:1:0.5), the Ag/CuO/Fe_3O_4/ACB composite achieved a remarkable CV removal efficiency of 98% within 90 min. Even after five consecutive reuse cycles, the composite retained a high degradation efficiency of 83%, demonstrating excellent stability and reusability. Comprehensive structural analyses

http://doi.org/10.58334/vrtc.jtst.n39.748

by XRD, FTIR, SEM, TEM, and VSM confirmed the successful formation and stability of the composite. This work not only offers a simple, eco-friendly approach to producing high-performance photocatalysts but also highlights the potential of using agricultural by-products for sustainable environmental remediation. The Ag/CuO/Fe_3O_4/ACB composite is a promising candidate for large-scale wastewater treatment and provides a strategic solution to combat organic dye pollution.

- Keywords*: Heterogeneous catalyst, activated carbon beads, Brucea javanica, crystal violet, heterogeneous photo-Fenton-like degradation*

1. INTRODUCTION

Water pollution from organic dyes poses a significant environmental issue due to their toxicity, persistence, and aesthetic impact on aquatic ecosystems. Dyes, particularly those used in the textile and printing industries, can hinder photosynthesis in aquatic ecosystems and pose serious health risks to humans and animals due to their mutagenic and carcinogenic properties [1, 2]. Various methods have been developed for dye removal, including biological treatments, membrane filtration, adsorption, and advanced oxidation processes (AOPs) [3-6]. Among these, the Fenton process and its modified form, the heterogeneous photo-Fenton-like process, have gained considerable attention due to their high efficiency in generating hydroxyl radicals (•OH) under light irradiation [7]. However, traditional Fenton systems suffer from limitations, including difficulty in catalyst recovery, metal ion leakage, and the need for acidic conditions [8].

In recent years, heterogeneous catalysts based on metal oxides such as Fe_3O_4, CuO, and Ag have been explored to overcome these limitations [9, 10]. Magnetite (Fe_3O_4) is widely used due to its magnetic properties, allowing easy recovery. However, Fe_3O_4 alone may exhibit limited catalytic performance. To enhance efficiency, composite materials have been developed by combining Fe_3O_4 with other metal oxides (CuO) and noble metals (Ag), which improve light absorption, charge separation, and reusability [11-13]. Silver (Ag) offers plasmonic effects for enhanced light absorption and antimicrobial properties, while CuO contributes to reactive species generation.

Despite these advances, existing photocatalysts often require complex synthesis methods, have limited stability, and face challenges in recovery. To address these issues, we developed a one-step synthesized composite, Ag/CuO/Fe_3O_4/activated carbon beads (ACB), using natural seeds of *Brucea javanica*. This approach is environmentally friendly, cost-effective, and simplifies the synthesis process. *Brucea javanica* seeds were chosen due to their natural porous structure, high carbon content, and sustainability as an agricultural by-product. The one-step carbonization method ensures strong adhesion of catalytic components to the carbon structure, enhancing stability and reusability. The resulting composite benefits from the synergistic effects of its components: (i) Ag enhances visible light absorption and provides antimicrobial activity; (ii) CuO generates reactive species for dye degradation; (iii) Fe_3O_4 facilitates magnetic recovery; and (iv) the carbon support increases adsorption capacity. This

unique structure addresses the common issues of limited light absorption, catalyst agglomeration, and difficult recovery.

In this study, the synthesized Ag/CuO/Fe_3O_4/ACB was applied for the heterogeneous photo-Fenton-like degradation of crystal violet (CV), a widely used and highly toxic dye. CV is challenging to degrade due to its complex aromatic structure and strong light absorption properties [14, 15]. Our study focuses on evaluating the composite's efficiency in CV degradation, reusability, and the effects of various operational parameters such as catalyst dosage, solution pH, and initial dye concentration.

2. MATERIALS AND METHODS

2.1. Materials

The main chemicals used in this study include silver nitrate ($AgNO_3$, ≥ 99.8%), iron (III) nitrate nonahydrate ($Fe(NO_3)_3.9H_2O$, ≥ 98%), copper (II) nitrate trihydrate ($Cu(NO_3)_2.3H_2O$, ≥ 98%), hydrogen peroxide (H_2O_2, 30% w/v), and Crystal Violet ($C_{25}H_{30}N_3Cl.xH_2O$, ≥ 95%), all of which were purchased from Sigma-Aldrich (Singapore). These chemicals were of analytical grade and used without further purification. Additionally, other general laboratory chemicals and reagents were used as needed, including ethanol (C_2H_5OH, ≥ 99.9%), sodium hydroxide (NaOH, ≥ 98%), hydrochloric acid (HCl, 37% w/w) and deionized water. *Brucea javanica* seeds were collected from the Da Nang region, Vietnam. The seeds were carefully washed with tap water to remove surface impurities, manually separated from their outer shells, and dried at 60°C.

2.2. Synthesis of Ag/CuO/Fe_3O_4/ACB

The Ag/CuO/Fe_3O_4/ACB composite was synthesized via a one-step carbonization method. Precisely, 1.5 g of $Fe(NO_3)_3 \cdot 9H_2O$, 0.45 g of $Cu(NO_3)_2 \cdot 6H_2O$, and 0.16 g of $AgNO_3$ were weighed to achieve a fixed molar ratio of Fe^{3+}:Cu^{2+}:Ag^+ = 2:1:0.5. These metal salts were dissolved in 50 mL of deionized water under continuous stirring to form a homogeneous solution. Subsequently, 5 g of pre-dried *Brucea javanica* seeds were added to the solution, and the mixture was stirred continuously at 65°C for 24 hours to facilitate the impregnation of metal ions into the porous structure of the seeds. After impregnation, the mixture was gently evaporated to near dryness at 65°C under stirring to ensure maximum adsorption of metal salts onto the seed surface. The resulting solid was then air-dried at room temperature to remove residual moisture. The impregnated seeds were then placed in a covered ceramic crucible and subjected to a thermal treatment at 500°C for 1 hour with a controlled heating ramp of 10°C/min in a muffle furnace under a limited oxygen environment (carbonization). The resulting composite material was subsequently washed sequentially with 50% ethanol (C_2H_5OH) and deionized water to remove any residual impurities. The clean composite was then oven-dried at 60°C overnight and stored in a sealed container for further use. Control samples were also prepared by the same method with the same mass ratio using only $AgNO_3$, $Fe(NO_3)_3$, $Cu(NO_3)_2$ or simultaneously $Fe(NO_3)_3$, $Cu(NO_3)_2$. The products are denoted respectively as Ag/ACB, Fe_3O_4/ACB, CuO/ACB, and CuO/Fe_3O_4/ACB.

2.3. Characterization methods

The structural, morphological, and compositional characteristics of the Ag/CuO/Fe_3O_4/ACB composite were characterized using multiple analytical techniques. X-ray diffraction (XRD) was performed on a Shimadzu XRD-6100 (Japan) with CuKα radiation (λ = 1.5406 Å) to identify the crystal phases. The surface morphology and elemental composition were analyzed by field emission scanning electron microscopy (FE-SEM) coupled with energy-dispersive X-ray spectroscopy (EDX) using a Hitachi S-4800 (Japan). High-resolution transmission electron microscopy (HR-TEM, JEM-2100, Japan) was employed to observe the internal structure and distribution of metal nanoparticles. The functional groups present on the composite surface were determined by Fourier Transform Infrared Spectroscopy (FTIR) using a a Tensor 27 spectrometer (Bruker, Germany), with spectra recorded in the range of 4000-400 cm^{-1}. The specific surface area and pore characteristics were measured using the Brunauer-Emmett-Teller (BET) method on a NOVA 1200e analyzer (Quantachrome, USA). Optical properties were assessed using UV-Vis diffuse reflectance spectroscopy (UV-Vis DRS) on a Shimadzu UV-2401 PC (Japan). Magnetic properties were investigated using a Vibrating Sample Magnetometer (VSM-DMS 880, USA), providing information on the magnetic behavior of the composite.

2.4. Photocatalytic-Fenton degradation experiments

The photocatalytic degradation of CV was carried out using a custom-designed photocatalytic system consisting of a 500 W halogen lamp (λ ≥ 420 nm), a light filter, a mechanical stirrer, a thermostatic water bath, and a three-necked glass reactor to ensure stable reaction conditions. A specified amount of the Ag/CuO/Fe_3O_4/ACB composite was dispersed in 100 mL of CV solution with an initial concentration of 20 mg/L. All samples were kept in the dark for 60 min to allow for initial dye adsorption assessment prior to visible-light irradiation. The reaction was initiated by turning on the light source, and the CV concentration was monitored at its maximum absorbance wavelength of 585 nm using a UV-Vis spectrophotometer (Cary 60, Agilent, USA). The influence of various operational parameters on the degradation efficiency was systematically studied. Specifically, the catalyst dosage was varied between 0.5 and 3 g/L, while the initial concentration of CV was adjusted between 15 and 30 mg/L. The concentration of hydrogen peroxide (H_2O_2) was controlled in the range of 0.025 to 0.1 M, and the solution pH was adjusted between 3 and 9 using HCl or NaOH solutions. The reaction temperature was maintained between 25 and 55°C using a thermostatic water bath. These conditions were optimized to identify the most effective degradation performance of the Ag/CuO/Fe_3O_4/ACB composite. At regular intervals, 2 mL aliquots of the reaction solution were withdrawn, immediately filtered to separate the catalyst, and the residual CV concentration was measured. The removal efficiency (R, %) and the apparent reaction rate constant (k) were calculated using the following equations:

$$R = \frac{C_t}{C_0} \times 100 \quad (1)$$

$$\mathrm{Ln}\frac{C_t}{C_o} = -kt \qquad (2)$$

where C_o (mg/L) is the initial concentration of CV, C_t (mg/L) is the concentration of CV at time t (min), and k (1/min) is the pseudo-first-order reaction rate constant obtained from the slope of the linear plot of LnC_t/C_o versus t.

The reusability of the Ag/CuO/Fe_3O_4/ACB composite was also evaluated under optimized conditions. Five consecutive degradation cycles were carried out; after each cycle, the catalyst was magnetically separated, the supernatant decanted, and the recovered solids were washed sequentially with distilled water and ethanol and then dried at 60 °C for 12 h to obtain dried catalyst granules, which were gently homogenized and reused in the subsequent cycle. Reusability was assessed by comparing the degradation efficiency at a fixed reaction time across cycles. Structural integrity and surface chemistry before and after reuse were examined by XRD and FTIR, and overall stability was inferred from sustained removal efficiency together with the preservation of the characteristic XRD/FTIR features.

3. RESULTS

3.1. Structural characterization (XRD)

The crystalline structure of the synthesized materials, including ACB, Fe_3O_4/ACB, CuO/Fe_3O_4/ACB, and Ag/CuO/Fe_3O_4/ACB, was analyzed using XRD, with the corresponding patterns shown in Fig. 1.

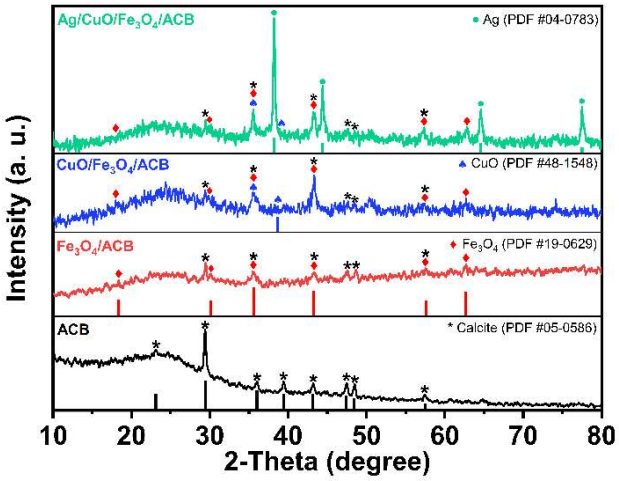

Figure 1. XRD patterns of ACB, Fe_3O_4/ACB, CuO/Fe_3O_4/ACB and Ag/CuO/Fe_3O_4/ACB

For the ACB sample, a distinct diffraction peak at $2\theta \approx 23.1°$ was observed, which corresponds to the (002) plane of amorphous carbon, confirming the carbonaceous nature of the material. Additionally, several diffraction peaks were identified at 29.4°, 35.9°, 39.4°, 43.2°, 47.5°, and 48.5°, which are attributed to the (104), (110), (113),

(202), (024), (116), (211), and (122) planes of calcite ($CaCO_3$) (PDF #05-0586) [16]. The Fe_3O_4/ACB composite shows characteristic peaks at 2θ values of 30.1°, 35.5°, 43.3°, 57.6°, and 62.7°, corresponding to the (220), (311), (400), (511), and (440) crystal planes of magnetite (Fe_3O_4) (JCPDS No. 19-0629) [17].

The XRD pattern of CuO/Fe_3O_4/ACB shows additional diffraction peaks at 2θ values of 35.5° and 38.7°, indicating the monoclinic phase of CuO (PDF #48-1548) [18]. This indicates that CuO is successfully formed and well-dispersed on the Fe_3O_4/ACB composite. In the case of Ag/CuO/Fe_3O_4/ACB, new diffraction peaks appear at 2θ values of around 38.1°, 44.3°, 64.4°, and 77.3°, corresponding to the face-centered cubic (FCC) structure of metallic silver (Ag) (PDF #04-0783) [19].

The gradual addition of CuO and Ag on the Fe_3O_4/ACB composite is evident from the increased intensity of the corresponding peaks in the XRD patterns.

The FTIR spectra of ACB, Fe_3O_4/ACB, CuO/Fe_3O_4/ACB, and Ag/CuO/Fe_3O_4/ACB are presented in Fig. 2, revealing the functional groups present on the surface of the synthesized materials.

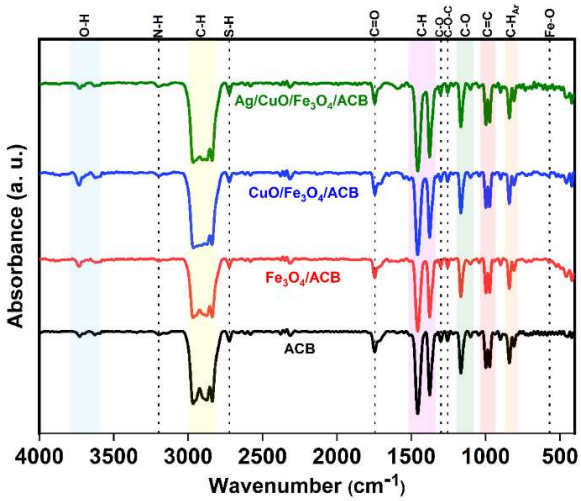

Figure 2. FTIR spectra of the synthesized samples

A sharp absorption band observed between 3730-3610 cm^{-1} is assigned to the stretching vibrations of isolated -OH groups on the surface of metal oxides or oxidized carbon. The bands observed around 1456 and 1377 cm^{-1} are attributed to the bending vibrations of C-H bonds in methyl (-CH_3) and methylene (-CH_2) groups, indicating the presence of organic carbon-based structures. Additionally, the peaks at ~2966, ~2939, and ~2850 cm^{-1} are attributed to the asymmetric and symmetric C–H stretching of –CH_3 and –CH_2– groups in aliphatic chains [21]. A notable feature is the appearance of a peak around 2723 cm^{-1}, particularly evident in the Ag/CuO/Fe_3O_4/ACB sample. The bands at 1303 and 1255 cm^{-1} correspond to C–O stretching and asymmetric C–

O–C stretching vibrations, characteristic of ester and ether groups. Finally, the characteristic peak at 570 cm^{-1} observed in the Fe_3O_4/ACB, CuO/Fe_3O_4/ACB, and Ag/CuO/Fe_3O_4/ACB samples is assigned to the Fe-O stretching vibrations, confirming the presence of magnetite (Fe_3O_4) in the composite.

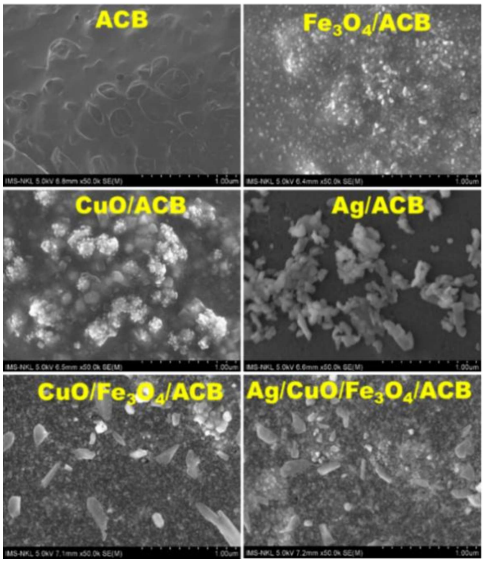

Figure 3. FE-SEM image of ACB, Fe_3O_4/ACB, Ag/ACB, CuO/Fe_3O_4/ACB and Ag/CuO/Fe_3O_4/ACB

The surface morphology of the synthesized composites was studied using FE-SEM, and the corresponding images are presented in Fig. 3. The FE-SEM image of ACB reveals a relatively smooth surface with visible porous structures, characteristic of carbonized biomass.

Upon the introduction of Fe_3O_4, the surface of the Fe_3O_4/ACB composite becomes significantly rougher, with numerous fine, spherical nanoparticles uniformly distributed across the carbon matrix. These particles are attributed to Fe_3O_4, which is effectively anchored on the ACB support. Further modification with CuO leads to a dramatic change in morphology, as seen in the CuO/ACB and CuO/Fe_3O_4/ACB samples. The surface becomes densely covered with clustered and agglomerated CuO particles, creating a rough and textured appearance. The addition of silver further transforms the surface morphology, as observed in the Ag/ACB and Ag/CuO/Fe_3O_4/ACB composites. Silver nanoparticles appear as bright, irregularly shaped clusters distributed across the carbon surface. In the Ag/CuO/Fe_3O_4/ACB composite, the SEM image reveals a complex multi-component structure where flake-like CuO, spherical Fe_3O_4, and clustered Ag coexist.

The morphology, elemental composition, and distribution of the Ag/CuO/Fe_3O_4/ACB composite were further characterized using TEM and EDX, as shown in Fig. 4.

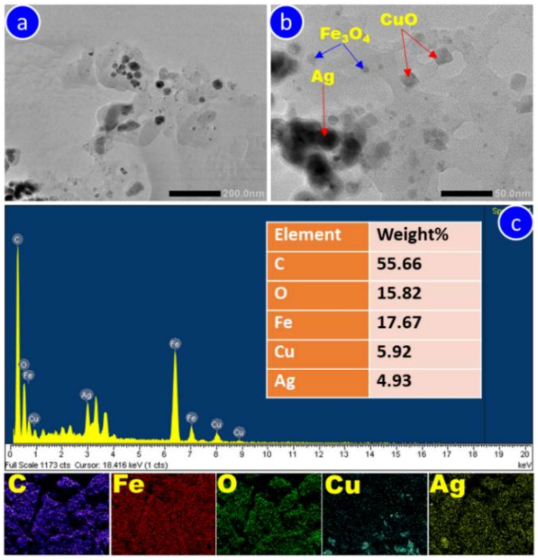

Figure 4. TEM (a, b) and EDX analysis (c) of Ag/CuO/Fe_3O_4/ACB composite

The TEM images (Fig. 4a-b) reveal a heterogeneous distribution of nanoparticles on the carbon matrix. In Fig. 4a, the low-magnification TEM image displays the overall morphology of the composite, where metal nanoparticles appear as dark spots distributed on the carbon surface. At higher magnification (Fig. 4b), the distinct morphology of the three components is clearly visible: Fe_3O_4 appears as bright, spherical nanoparticles (~10 nm), CuO is observed as well-defined cubic particles (20 nm), and Ag is present as bigger (25 nm), darker spherical particles. The elemental composition of the composite was further validated by EDX analysis (Fig. 4c), which shows strong signals for carbon (C), oxygen (O), iron (Fe), copper (Cu), and silver (Ag), consistent with the expected composition of Ag/CuO/Fe_3O_4/ACB. The EDX analysis reveals that the composite is predominantly composed of carbon (55.66%), along with oxygen (15.82%), iron (17.67%), copper (5.92%), and silver (4.93%).

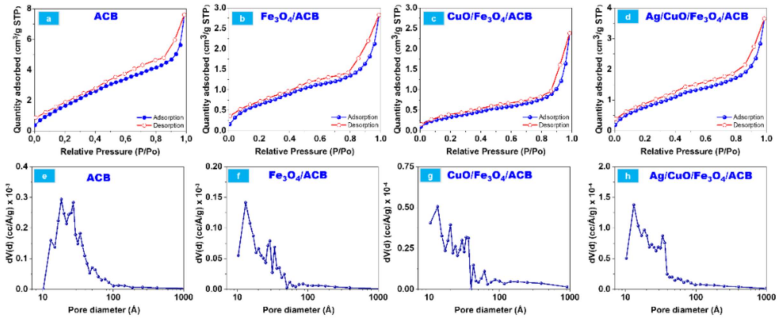

Figure 5. N_2 adsorption-desorption isotherms (a-d) and pore size distribution (e-h) of (a, e) ACB, (b, f) Fe_3O_4/ACB, (c, g) CuO/Fe_3O_4/ACB, and (d, h) Ag/CuO/Fe_3O_4/ACB composites

Table 1. Textural properties of ACB and metal-loaded ACB composites.

Sample	S_{BET} (m^2/g)	Pore volume* (cm^3/g)	Pore diameter* (nm)
ACB	7.98	0.014	1.83
Fe_3O_4/ACB	2.51	0.005	1.32
CuO/Fe_3O_4/ACB	1.30	0.004	1.33
Ag/CuO/Fe_3O_4/ACB	3.11	0.007	1.32

The textural properties of the synthesized samples were characterized by N_2 adsorption-desorption isotherms and pore size distribution, as shown in Fig. 5. The specific surface area (SBET), pore volume, and average pore diameter of the samples are summarized in Table 1. The N_2 adsorption-desorption isotherms (Fig. 5a-5d) of all samples exhibit Type IV-like features with H3-type hysteresis loops, typically associated with slit-shaped pores in non-rigid aggregates.

Upon loading with Fe_3O_4, the specific surface area of Fe_3O_4/ACB decreases significantly to 2.51 m^2/g, accompanied by a slight reduction in pore volume (0.005 cm^3/g).

In the case of Ag/CuO/Fe_3O_4/ACB, a slight increase in surface area (3.11 m^2/g) and pore volume (0.007 cm^3/g) is observed compared to CuO/Fe_3O_4/ACB. The optical and magnetic properties of the synthesized composites were characterized by UV-Vis (DRS) and VSM, respectively, as shown in Fig. 6.

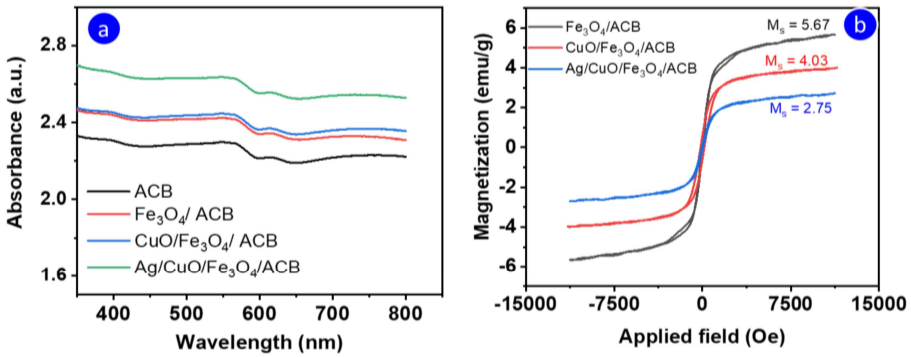

Figure 6. (a) UV-Vis DRS and (b) magnetization curves of the synthesized samples

The UV-Vis DRS spectra (Fig. 6a) reveal that all samples exhibit absorption in the visible region with slight variations in intensity. The magnetic properties of the samples were evaluated using VSM, and the magnetization curves are presented in Fig. 6b. The Fe_3O_4/ACB composite exhibits a saturation magnetization (Ms) of 5.67 emu/g, which is attributed to the presence of Fe_3O_4 nanoparticles. The addition of CuO in the CuO/Fe_3O_4/ACB composite reduces the Ms value to 4.03 emu/g, indicating that the non-magnetic CuO dilutes the magnetic effect of Fe_3O_4. In contrast, the Ag/CuO/Fe_3O_4/ACB composite shows a further decrease in Ms to 2.75 emu/g, possibly due to the increased presence of non-magnetic Ag, which reduces the overall magnetic response of the material.

3.2. Effect of operational parameters on catalytic performance

In this study, the effects of key operational parameters on the photocatalytic degradation of CV using the Ag/CuO/Fe_3O_4/ACB composite were systematically investigated, as shown in Fig. 7.

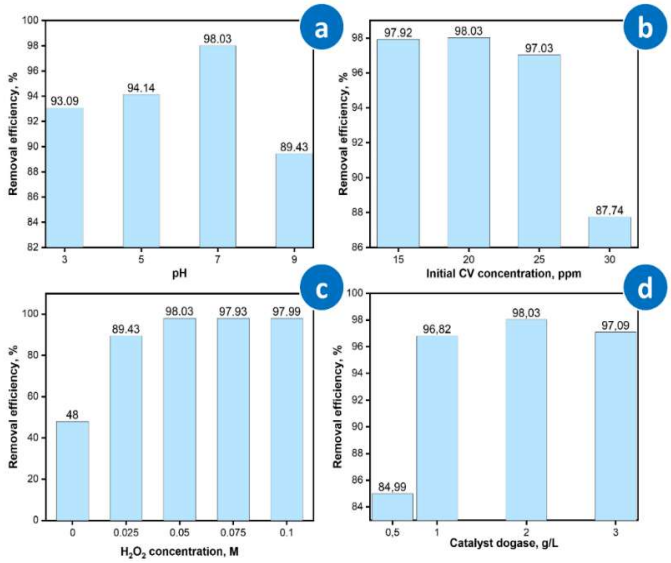

Figure 7. Effect of operational parameters on the photocatalytic degradation of CV using Ag/CuO/Fe_3O_4/ACB composite: (a) pH, (b) initial CV concentration, (c) H_2O_2 concentration, and (d) catalyst dosage.

The degradation efficiency of CV is significantly affected by the solution pH, ranging from 3 to 9 (Fig. 7a). The highest removal efficiency is achieved at pH 7, reaching approximately 98% within 90 min. The effect of CV dye concentration on its initial degradation using the Ag/CuO/Fe_3O_4/ACB catalyst system was investigated, and the results are presented in Fig. 7b. As shown, for initial CV concentrations ranging from 15-25 ppm after 90 minutes of reaction, the CV removal efficiency all reached > 97% and achieved a maximum value of 98.03% at a CV concentration of 20 ppm. When the initial CV concentration was further increased to 30 ppm, the degradation efficiency decreased significantly to 87.74%. The role of H_2O_2 in the heterogeneous photo-Fenton-like process is highlighted in Fig. 7c. The degradation efficiency improves with increasing H_2O_2 concentration from 0.025 M to 0.05 M, reaching a maximum of approximately 98.03%. The catalyst dosage was varied between 0.5 g/L to 3 g/L, and its influence on CV degradation is shown in Fig. 7d. The degradation efficiency increases with higher catalyst dosage, reaching an optimum at 2 g/L.

3.3. Catalytic performance comparison and kinetic study

The catalytic performance of the synthesized materials was evaluated through the photodegradation of CV under various conditions, as illustrated in Fig. 8.

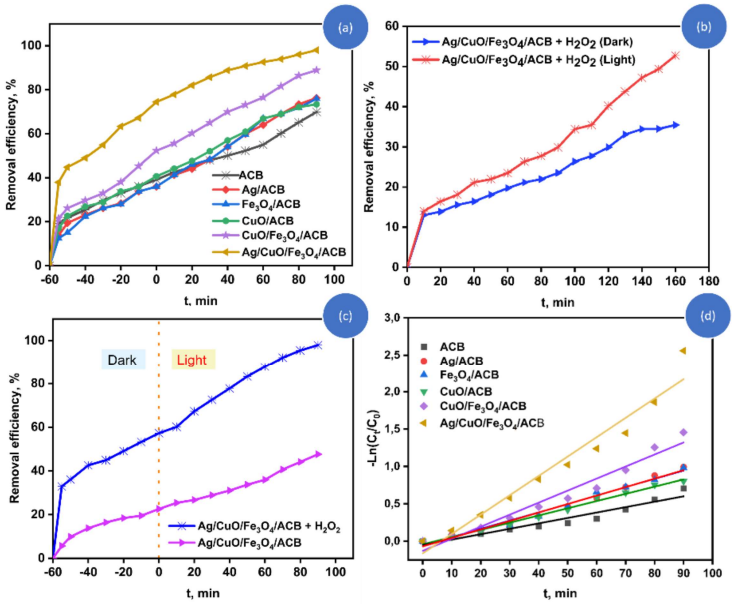

Figure 8. Catalytic performance of the synthesized materials in CV degradation: (a) CV removal efficiency of different catalysts; (b) Comparison of degradation efficiency of Ag/CuO/Fe_3O_4/ACB under light and dark conditions; (c) Effect of H_2O_2 on the photodegradation of CV using Ag/CuO/Fe_3O_4/ACB; (d) Pseudo-first-order kinetic plots for the CV degradation process.

(*Experimental condition: [CV] = 20 mg/L, pH = 7, T = 25°C, [H_2O_2] = 0.05 M).*

Fig. 8a compares the CV removal efficiency of the synthesized materials, including ACB, Ag/ACB, Fe_3O_4/ACB, CuO/ACB, CuO/Fe_3O_4/ACB, and Ag/CuO/Fe_3O_4/ACB.

Among these, the Ag/CuO/Fe_3O_4/ACB composite demonstrates the highest degradation efficiency, reaching 98% within 90 min under light irradiation. In contrast, the ACB sample shows the lowest catalytic activity, achieving only around 70% CV removal. The Ag/ACB, Fe_3O_4/ACB, and CuO/ACB samples show moderate activities (73-88%), demonstrating the individual contributions of Ag, Fe_3O_4, and CuO in enhancing catalytic performance. The impact of light on the catalytic performance of the Ag/CuO/Fe_3O_4/ACB composite was further investigated under light and dark conditions, as shown in Fig. 8b. In the dark, the degradation efficiency is significantly lower, achieving only around 36% CV removal after 160 min. Under light irradiation, the degradation efficiency is dramatically enhanced, reaching approximately 53% within the same period. Fig. 8c compares the degradation efficiency of Ag/CuO/Fe_3O_4/ACB with and without H_2O_2. Both systems were pre-equilibrated in the dark for 60 minutes to achieve adsorption equilibrium, followed by light irradiation. In the absence of H_2O_2, the Ag/CuO/Fe_3O_4/ACB composite exhibits limited catalytic activity, achieving less than 50% CV removal. However, with the addition of H_2O_2 (0.05 M), the degradation efficiency significantly increases, reaching 98%.

The kinetics of CV degradation were further analyzed using a pseudo-first-order kinetic model, and the corresponding kinetic constants (k_1) and correlation coefficients (R^2) are summarized in Table 2.

Table 2. Kinetic parameters of CV photodegradation using different catalysts

Sample	k_1 (min^{-1})	R^2
ACB	0.0061	0.964
Ag/ACB	0.0072	0.760
CuO/ACB	0.0079	0.979
Fe_3O_4/ACB	0.0084	0.966
CuO/Fe_3O_4/ACB	0.0124	0.959
Ag/CuO/Fe_3O_4/ACB	0.0188	0.986

The Ag/CuO/Fe_3O_4/ACB composite exhibits the highest reaction rate constant (k_1 = 0.0188 min^{-1}, R^2 = 0.986), significantly higher than those of other samples. The catalytic performance of Ag/CuO/Fe_3O_4/ACB was further assessed by comparing its efficiency in CV degradation with other reported photocatalysts under similar conditions (Table 3). As shown, the degradation efficiency varied from 67% to 98.03% depending on the catalyst type and reaction conditions. Notably, Ag/CuO/Fe_3O_4/ACB achieved the highest CV removal efficiency (98.03% in 90 min), outperforming systems such as HC-TiO_2, Ag_2MoO_4/MIL-101(Fe)/Ag and ZnO-based materials.

Table 3. CV photodegradation with different catalysts in aqueous solution

Catalyst	Experimental conditons: [CV], catalyst dosage, [H_2O_2]	Type of reaction	Time (min)	R (%)	Ref.
ZnO/Clay (ZnO/CNA)	50 mg/L; 0.5 g/L; -	Photocatalytic	120	~92	[23]
Ag_2MoO_4/MIL-101(Fe)/Ag	25 mg/L; 2 g/L; 50 mM	Heterogeneous photo-Fenton-like-like	90	~97	[15]
TiO_2 (P-25)	15 mg/L; 0.1 g/L; -	Photocatalytic	60	~67	[24]
ZnO nanoparticles	30 mg/L; 1 g/L; -	Photocatalytic	120	~70	[25]
HC-TiO_2 (hydrochar/TiO_2)	20 mg/L; 1 g/L; -	Photocatalytic	90	77	[26]
Ag/CuO/Fe_3O_4/ACB	20 mg/L; 2 g/L; 50 mM	Heterogeneous photo-Fenton-like	90	98.03	This study

3.4. Reusability of Ag/CuO/Fe_3O_4/ACB composite

The reusability of the Ag/CuO/Fe_3O_4/ACB composite was evaluated over five consecutive degradation cycles of CV, and the results are shown in Fig. 9. The initial removal efficiency of 98% gradually decreases with repeated use, reaching approximately 83% after five cycles (Fig. 9a).

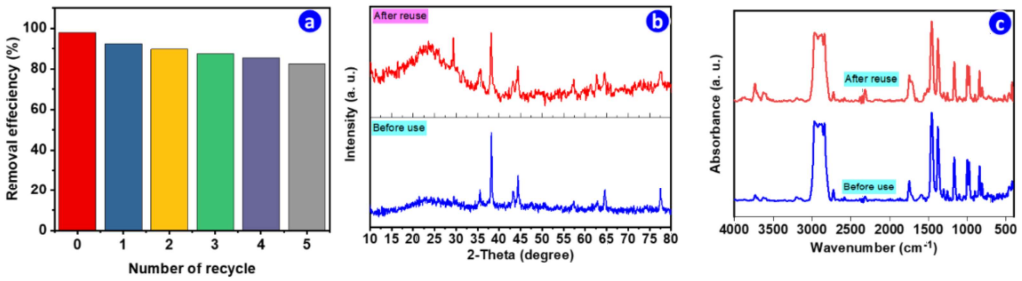

Figure 9. Reusability and stability of the Ag/CuO/Fe_3O_4/ACB composite: (a) catalytic performance over five consecutive cycles of CV degradation; (b) XRD patterns before and after reuse; (c) FTIR spectra before and after reuse

The structural stability of the composite was further assessed using XRD (Fig. 9b) and FTIR (Fig. 9c) analyses before and after reuse. The XRD patterns (Fig. 9b) show that the main diffraction peaks corresponding to Fe_3O_4, CuO, and Ag remain identifiable after five cycles, indicating the retention of the primary crystalline phases. However, noticeable broadening of the peaks, especially in the $2\theta < 30°$ region, was observed after reuse. Although a slight decrease in the intensity of characteristic functional groups is observed, indicating minor surface modification, the main functional groups remain intact.

4. DISCUSSION

4.1. Crystal structure and surface functional groups (XRD/FTIR)

The presence of calcite is likely due to the natural mineral content of the *Brucea javanica* seeds, which remains stable even after carbonization. The characteristic Fe_3O_4 reflections confirms the successful formation of magnetic Fe_3O_4 nanoparticles on the activated carbon support. The appearance of CuO-specific peaks indicates that CuO is successfully formed and well-dispersed on the Fe_3O_4/ACB composite. The presence of Ag-related peaks peaks confirms the successful formation of silver nanoparticles in the composite. The combination of Ag, CuO, and Fe_3O_4 is clearly observed in this composite, indicating a successful synthesis of the Ag/CuO/Fe_3O_4/ACB composite.

The absence of any other impurity peaks suggests high purity and successful synthesis of the composite materials. These FTIR peaks are typically associated with non-hydrogen-bonded hydroxyls [20]. The pronounced band at 1747 cm^{-1} corresponds to the C=O stretching vibrations of carbonyl groups, likely derived from ester or ketone functionalities formed during the carbonization process. These FTIR

bands are consistent across all samples, confirming the carbonaceous nature of the ACB substrate.

A distinct absorption peak around 3197 cm^{-1} is associated with the stretching vibrations of N-H groups, suggesting the retention of nitrogen-containing organic residues from the natural precursor (*Brucea javanica* seeds). These spectroscopic features confirm the presence of residual alkyl functionalities within the ACB matrix and its metal-loaded composites. The ~2723 cm^{-1} peak can be attributed to the stretching vibration of thiol (-SH) groups, indicating possible interactions between thiol groups and metallic nanoparticles (Ag), which may enhance the catalyst's stability and performance. These functional groups are typically associated with the organic matrix derived from the natural precursor. The region between 1166 and 1099 cm^{-1} further confirms the presence of C-O-C linkages, which are indicative of polysaccharide or ether structures, consistent with the organic carbon backbone of ACB. Distinct absorption peaks at 997 and 972 cm^{-1}, particularly noticeable in the Ag/CuO/Fe_3O_4/ACB sample, are attributed to C=C bending vibrations, suggesting the existence of aromatic structures. These aromatic-related peaks may be enhanced by the surface plasmon resonance (SPR) effect of Ag nanoparticles, which can amplify the infrared absorption signals. This peak is a clear indicator of the successful incorporation of Fe_3O_4 into the composite structure.

This FTIR analysis confirms the successful synthesis of the composite materials, with each functional group providing insights into the chemical interactions between the carbonaceous substrate, metal oxides, and metallic silver.

4.2. Morphological and elemental analysis (SEM, EDX, TEM)

These biomorphic pores, inherited from the natural structure of Brucea javanica seeds, provide a high surface area, which is favorable for the subsequent loading of metal oxides. The homogeneous distribution of these magnetic nanoparticles suggests efficient impregnation and in-situ formation during the carbonization process, which is crucial for achieving magnetic properties. The observed aggregation is characteristic of CuO, which tends to form granular or flower-like structures.

In the CuO/Fe_3O_4/ACB composite, the coexistence of spherical Fe_3O_4 and granular CuO particles is clearly visible, indicating the successful integration of both metal oxides. This heterostructure is expected to enhance catalytic performance by combining the magnetic properties of Fe_3O_4 with the active sites of CuO. This unique morphology, characterized by a combination of rough and heterogeneous features, is indicative of successful multi-metal loading. Such a structure is advantageous for photocatalysis, as it provides a high density of active sites and facilitates the interaction between Ag, CuO, and Fe_3O_4. The distinct contrast and morphology observed in the TEM images suggest the presence of Fe_3O_4, CuO, and Ag phases with differentiable shapes or sizes, likely due to their intrinsic structural features. Overall, the images support the successful co-loading of these phases onto the carbon matrix with retained structural integrity.

Based on the EDX values, the estimated molar ratio of Fe:Cu:Ag is approximately 3.5:1:0.5, which is in reasonable agreement with the intended synthesis ratio of 2:1:0.5. The deviations may arise due to several factors, such as the surface-sensitive nature of EDX analysis, potential preferential deposition, or enrichment of metal species at the surface, and partial loss or redistribution of elements during high-temperature carbonization. The corresponding element mapping images further confirm the homogeneous distribution of Fe, Cu, and Ag on the carbon matrix, supporting the successful incorporation of all three active components into the composite structure.

4.3. Surface area, porosity analysis, optical and magnetic properties

Although these H3-type hysteresis loops are commonly observed in mesoporous materials, the measured pore diameters (1.3-1.8 nm) indicate that the composites are predominantly microporous, based on IUPAC classification. This apparent mismatch may result from narrow slit-like pores or surface heterogeneity in the carbon matrix, which can produce H3-type hysteresis even in microporous structures. Among them, ACB shows the highest specific surface area (7.98 m^2/g) and the largest pore volume (0.014 cm^3/g), which can be attributed to the porous carbon structure derived from *Brucea javanica* seeds.

The pore size distribution (Fig. 5e-5h) further confirms the dominance of mesopores in ACB. This decline in surface area and pore volume is attributed to the partial blockage of the carbon pores by the Fe_3O_4 nanoparticles. The average pore diameter also decreases to 1.32 nm, indicating the formation of Fe_3O_4 particles within the mesopores of ACB. The CuO/Fe_3O_4/ACB composite shows a further reduction in specific surface area (1.30 m^2/g) and pore volume (0.004 cm^3/g), suggesting that the loading of CuO further blocks the porous structure.

However, the average pore diameter remains relatively constant (1.33 nm), indicating that CuO primarily occupies the existing mesopores rather than forming new pore structures. This slight increase in surface area may be associated with the presence of Ag nanoparticles, which could influence the surface texture or local porosity. Although all metal components were co-loaded during the one-step carbonization, the addition of Ag may help preserve certain surface features or reduce pore collapse, thereby contributing to a marginal increase in SBET without significantly affecting the average pore diameter. The ACB sample shows minimal absorption, consistent with its carbonaceous nature. Fe_3O_4/ACB displays a broader absorption profile, typical of Fe_3O_4 as a narrow band gap semiconductor. The addition of CuO enhances light absorption modestly, and a further increase is observed in the Ag/CuO/Fe_3O_4/ACB composite, which may be attributed to the surface plasmon resonance (SPR) effect of Ag nanoparticles. Although the absolute differences in absorbance values are relatively small, the trend suggests a gradual improvement in visible light responsiveness upon metal incorporation.

As expected, ACB is non-magnetic, showing no detectable magnetic response. The moderate magnetization values of these composites, especially for

Ag/CuO/Fe_3O_4/ACB, are sufficient for magnetic recovery under an external magnetic field. This magnetic-separation feature is essential for the reusability of the catalyst, allowing for efficient separation from the reaction medium after use without requiring complex filtration or centrifugation.

4.4. Effects of reaction conditions

The optimization of operational parameters is a critical aspect in enhancing the performance of photocatalytic systems, particularly in Fenton-based processes where multiple factors simultaneously influence the generation of ROS, electron transfer efficiency, and interaction between the catalyst and pollutants. At pH 7, the heterogeneous photo-Fenton-like process is optimized due to efficient Fe^{3+}/Fe^{2+} redox cycling on the surface of Fe_3O_4 nanoparticles, which promotes the continuous generation of hydroxyl radicals. Although Fe^{3+} can hydrolyze to form $Fe(OH)_3$ at lower pH, the leached Fe^{3+} concentration from solid Fe_3O_4 in our system is minimal, and the redox activity primarily occurs at the catalyst surface. Thus, no significant precipitation interferes with the process at pH 7. At pH 5, the degradation performance is moderate but lower than at neutral pH, possibly due to suboptimal balance between H^+ availability and redox efficiency. At pH 3, excess H^+ competes with Fe^{2+}, suppressing •OH generation, while at pH 9, $Fe(OH)_3$ precipitation and insufficient H^+ both hinder the Fenton reaction.

Overall, the results indicate that neutral pH is the most favorable condition for the heterogeneous photo-Fenton-like degradation of CV using Ag/CuO/Fe_3O_4/ACB. This phenomenon can be explained as follows: At low CV concentrations (15-25 ppm), CV molecules are easily adsorbed and make good contact with the active sites on the catalyst surface, enhancing the degradation capability through •OH oxidizing radicals generated on the material surface.

Conversely, at CV concentrations higher than 25 ppm, the treatment efficiency decreases significantly because the number of CV molecules exceeds the adsorption capacity of the catalyst, causing saturation of the catalyst surface. Additionally, excess CV molecules may compete for or cover the active centers on the Ag/CuO/Fe_3O_4/ACB surface, limiting the formation and contact capability of oxidizing radicals (•OH) with CV molecules. Therefore, to optimize the CV treatment process using Ag/CuO/Fe_3O_4/ACB material, the initial CV concentration should be selected at 20 ppm, ensuring the highest treatment efficiency. At higher H_2O_2 concentrations (0.075 M and 0.1 M), the degradation efficiency remains nearly unchanged (~97.9–98%), suggesting a saturation point rather than a real decrease. Although excessive H_2O_2 can theoretically act as a •OH scavenger [22], this effect is not significant under our experimental conditions. Thus, 0.05 M H_2O_2 is considered the optimal concentration, balancing reagent usage and performance. This optimal performance is because an increased catalyst dosage provides more active sites for ROS generation and dye adsorption. However, a further increase to 3 g/L results in a slight decline in efficiency, likely due to particle aggregation, which reduces the available active surface area and increases light scattering, thus limiting photocatalytic activity.

4.5. Catalytic performance

The superior performance in CV photodegradation - 98% removal within 90 min at pH 7 with 0.05 M H_2O_2 under illumination, outperforming ACB, Ag/ACB, Fe_3O_4/ACB, and CuO/ACB is attributed to the synergistic effects of Ag, CuO, and Fe_3O_4. The Ag nanoparticles enhance light absorption through SPR, while CuO provides active sites for reactive oxygen species (ROS) generation, and Fe_3O_4 facilitates efficient electron transfer and magnetic recovery. This result for ACB is expected since ACB lacks active metal components and primarily relies on its limited adsorption capacity.

The limited activity under dark conditions is mainly due to the adsorption of CV onto the catalyst surface and the slow Fenton-like reaction. The improvement under illumination is attributed to the activation of the heterogeneous photo-Fenton-like process, where light energy promotes the generation of reactive oxygen species (•OH) through the combined effect of CuO, Ag, and Fe_3O_4. The Ag nanoparticles, in particular, enhance light absorption due to their SPR effect, while CuO and Fe_3O_4 serve as active centers for •OH production. This lower efficiency without H_2O_2 is because the primary degradation pathway is restricted to photolysis and photo-catalysis. H_2O_2 serves as a source of •OH radicals in the presence of the metal oxides, particularly Fe_3O_4, which facilitates the decomposition of H_2O_2 through a Fenton-like reaction.

The combination of light and H_2O_2 thus maximizes the generation of ROS, leading to efficient CV degradation. The linear plots of $-\ln(C_t/Co)$ versus time (Fig. 8d) confirm that the degradation process follows first-order kinetics. The improved kinetic performance of Ag/CuO/Fe_3O_4/ACB is attributed to the synergistic interactions among Ag, CuO, and Fe_3O_4, which collectively enhance light absorption, ROS generation, and electron transfer. This composite effectively combines the advantages of each component, resulting in superior photocatalytic activity. This excellent performance is attributed to the synergistic effect of Ag, CuO, and Fe_3O_4 in the heterogeneous photo-Fenton-like process, which enhances light absorption, reactive oxygen species generation, and catalyst recovery. These results underline the strong catalytic activity and application potential of Ag/CuO/Fe_3O_4/ACB for dye-contaminated wastewater treatment.

4.6. Proposed heterogeneous photo-Fenton mechanism for CV degradation

Under visible-light irradiation, decolorization is markedly accelerated in the presence of H_2O_2, whereas it remains limited without the oxidant; in the dark, the process is negligible. The Ag/CuO/Fe_3O_4@ACB composite also affords the largest pseudo-first-order rate constant among the tested materials. Optical characterization reveals an enhanced visible response attributable to Ag plasmonic effects, while structural/morphological analyses confirm the coexistence and intimate contact of Ag, CuO and Fe_3O_4 nanoparticles anchored on the carbon matrix. Taken together, these observations are consistent with a plasmon-assisted heterogeneous photo-Fenton pathway operating near neutral pH: CuO generates electron-hole pairs under visible

light; Ag acts as an electron sink (Schottky/LSPR), suppressing recombination and supplying hot electrons; Fe_3O_4 catalyzes the interfacial Fe^{2+}/Fe^{3+} cycle to activate H_2O_2; and the ACB matrix enriches CV near active sites and facilitates interfacial charge transfer.

A possible degradation mechanism is proposed, as described by eqn (3)–(11):

$$Ag/CuO/Fe_3O_4@ACB + h\nu\ (\lambda \geq 420\ nm) \rightarrow h_{VB}^{+} + e_{CB}^{-} \quad (3)$$

$$e_{CB}^{-} \rightarrow e_{Ag}^{-} \quad (4)$$

$$Fe^{3+} + e_{Ag}^{-} \rightarrow Fe^{2+} \quad (5)$$

$$Fe^{2+} + H_2O_2 \rightarrow Fe^{3+} + {}^{\bullet}OH + OH^{-} \quad (6)$$

$$Fe^{3+} + H_2O_2 \rightarrow Fe^{2+} + {}^{\bullet}O_2H + H^{+};\ {}^{\bullet}O_2H \rightleftharpoons H^{+} + {}^{\bullet}O_2^{-} \quad (7)$$

$$e_{Ag}^{-} + H_2O_2 \rightarrow {}^{\bullet}OH + OH^{-} \quad (8)$$

$$O_2 + e_{Ag}^{-} \rightarrow {}^{\bullet}O_2^{-} \quad (9)$$

$$h_{VB}^{+} + H_2O \rightarrow {}^{\bullet}OH + H^{+} \quad (10)$$

$$CV + ({}^{\bullet}OH/\ {}^{\bullet}O_2^{-}/h^{+}) \rightarrow \text{degradation products} \quad (11)$$

4.7. Stability and reusability

The slight reduction in catalytic activity after multiple cycles can be attributed to several interconnected factors. These include the partial deactivation of active sites due to prolonged exposure to oxidative conditions, as well as the agglomeration of metal nanoparticles, which reduces the available surface area for photocatalytic reactions. Additionally, the gradual leaching of metal ions-particularly Ag^{+} and Cu^{2+} - into the reaction medium during operation and washing steps may diminish the concentration of active components. Furthermore, surface fouling caused by the accumulation of dye degradation intermediates or byproducts may block active sites and hinder mass transfer, contributing to the observed decline in performance. This peak broadening may suggest a decrease in crystallite size. The reduction in crystallite size could be attributed to surface erosion caused by ROS generated during the heterogeneous photo-Fenton-like process, localized thermal or mechanical stress under light irradiation, or partial leaching and reprecipitation of metal ions in smaller crystalline domains.

The FTIR spectra (Fig. 9c) further confirm the chemical stability of the composite. The retention of the characteristic peaks for hydroxyl (-OH), carbonyl (C=O), and metal-oxygen bonds suggests that the carbon matrix and metal oxides are chemically stable. These results demonstrate that the $Ag/CuO/Fe_3O_4$/ACB composite maintains good catalytic activity and structural stability over multiple cycles, making it a promising candidate for practical applications in wastewater treatment.

5. CONCLUSION

In this study, a multifunctional Ag/CuO/Fe_3O_4/ACB composite was successfully synthesized using a one-step carbonization method from natural *Brucea javanica* seeds. The composite demonstrated excellent photocatalytic activity for the degradation of CV under visible light irradiation. The Ag/CuO/Fe_3O_4/ACB composite exhibited a well-defined hierarchical structure, with Ag, CuO, and Fe_3O_4 nanoparticles (10-25 nm) uniformly distributed on the porous carbon matrix. This unique architecture enhanced light absorption, charge separation, and reactive oxygen species generation, resulting in superior catalytic performance. The heterogeneous photo-Fenton-like degradation of CV was most efficient at pH 7, with an optimal H_2O_2 concentration of 0.05 M, and catalyst dosage of 2 g/L. Under these conditions, the Ag/CuO/Fe_3O_4/ACB composite achieved a CV removal efficiency of 98% within 90 min. The Ag/CuO/Fe_3O_4/ACB composite maintained high catalytic activity, with a CV removal efficiency of 83% after five consecutive reuse cycles. XRD and FTIR analyses confirmed that the composite retained its crystalline structure and chemical integrity after repeated use. This study lays a solid foundation for developing efficient, reusable, and environmentally friendly photocatalysts for wastewater treatment. Future work will focus on optimizing the composite structure for enhanced activity and exploring its applicability to other organic pollutants. In particular, testing the Ag/CuO/Fe_3O_4/ACB composite against a broader range of emerging contaminants such as antibiotics, pesticides, and industrial dyes will provide further insight into its versatility. Additionally, evaluating the catalyst performance in real wastewater matrices and continuous-flow systems is essential for assessing its practical potential in large-scale applications.

***Acknowledgements**: The authors express their gratitude to the Joint Vietnam - Russia Tropical Science and Technology Research Center for its support and encouragement. This research was funded by the Joint Vietnam - Russia Tropical Science and Technology Research Center (Project No. ĐB.Đ2.04/24).*

***Author contributions**: Viet Hung Hoang: Writing - original draft, Review & Editing, Methodology, Conceptualization. Van Thuan Le: Software, Resources, Formal analysis, Data curation, Writing - Review & Editing. Van Thanh Nguyen: Investigation/Experimentation, Formal analysis. Thi Thao Le, Minh Hieu Do: Investigation/Experimentation. Van Dat Doan: Investigation, Formal analysis, Visualization, Validation, Methodology.*

***Conflicts of interest statement**: The authors declare that they have no known competing financial interests or personal relationships that could have appeared to influence the work reported in this paper.*

REFERENCE

1. P. Rajapaksha, R. Orrell-Trigg, Y. B. Truong, D. Cozzolino, V. K. Truong and J. Chapman, *Wastewater depollution of textile dyes and antibiotics using unmodified and copper oxide/zinc oxide nanofunctionalised graphene oxide*

materials, Environmental Science*:* Advances, Vol. 1, pp. 456-469, 2022. DOI:10.1039/d2va00059h

2. J. Yang, S. Shojaei and S. Shojaei, *Removal of drug and dye from aqueous solutions by graphene oxide: Adsorption studies and chemometrics methods*, npj Clean Water 5, Vol. 5, pp. 1-10, 2022. DOI:10.1038/s41545-022-00148-3

3. D. Patel, A. Singh, S. R. Ambati, R. S. Singh and R. K. Sonwani, *An overview of recent advances in treatment of complex dye-containing wastewater and its techno-economic assessment*, Journal of Environmental Management, Vol. 370, p. 122804, 2024. DOI: 10.1016/j.jenvman.2024.122804

4. N. Vasiraja, S. P. R. Saravana, A. Joshua, S. M. Kennedy and R. Rb Jeen, *Sustainable Methylene Blue dye removal with activated carbon from Prosopis juliflora stem*, International Journal of Phytoremediation, Vol. 27, pp. 472-480, 2024. DOI: 10.1080/15226514.2024.2427377

5. Abdullah et al., *Green synthesis and characterization of copper and nickel hybrid nanomaterials: Investigation of their biological and photocatalytic potential for the removal of organic crystal violet dye*, Journal of Saudi Chemical Society, Vol. 26, p. 101486, 2022. DOI:10.1016/j.jscs.2022.101486

6. G. Mustafa et al., *Microalgal and activated sludge processing for biodegradation of textile dyes*, Environmental Pollution, Vol. 349, p. 123902, 2024. DOI:10.1016/j.envpol.2024.123902

7. C. Dong, M. Xing and J. Zhang, *Recent progress of photocatalytic fenton-like process for environmental remediation,* Frontiers in Environmental Chemistry, Vol. 1, p. 581269, 2020. DOI:10.3389/fenvc.2020.00008/xml/nlm

8. M. Li, J. Song, W. Han, K. L. Yeung, S. Zhou and C. H. Mo, *Iron-organic frameworks as effective fenton-like catalysts for peroxymonosulfate decomposition in advanced oxidation processes*, npj Clean Water, Vol. 6, pp. 1-10, 2023. DOI:10.1038/s41545-023-00251-z

9. V. T. Le et al., *Efficient photocatalytic degradation of crystal violet under natural sunlight using Fe_3O_4/ZnO nanoparticles embedded carboxylate-rich carbon,* Materials Letters, Vol. 283, p. 128749, 2021. DOI: 10.1016/j.matlet.2020.128749

10. B. Bai, G. Cheng, J. Chen, X. Chen and Q. Wang, *Strong magnetic p-n heterojunction Fe_3O_4-$FeWO_4$ for heterogeneous photo-Fenton-like degradation of tetracycline hydrochloride*, Catalysts, Vol. 14, p. 453, 2023. DOI:10.3390/catal14070453

11. V. T. Le, V. A. Tran, D. L. Tran, T. L. H. Nguyen and V. D. Doan, *Fabrication of Fe_3O_4/CuO@C composite from MOF-based materials as an efficient and magnetically separable photocatalyst for degradation of ciprofloxacin antibiotic,* Chemosphere, Vol. 270, pp. 129417, 2021. DOI:10.1016/j.chemosphere.2020.129417

12. F. Riyanti, P. L. Hariani, H. Hasanudin, A. Rachmat and W. Purwaningrum, *Optimization photodegradation of methylene blue dye using bentonite/PDA/ Fe_3O_4/CuO@C composite by response surface methodology*, Bulletin of Chemical Reaction Engineering & Catalysis, Vol. 19, pp. 252-264. DOI: 10.9767/bcrec.20132

13. A.E. Khyave, R. Mafigholmi, A. Davood, A. Mahvi and L. Salimi, *Photocatalytic degradation of azithromycin and ceftriaxone using synthesized Ag/g-C_3N_4/Fe_3O_4 nanocomposites in aqueous solution*, Scientific Reports, Vol. 15, pp. 18726, 2025. DOI: 10.1038/s41598-025-00149-5

14. V. D. Doan, V. T. Le, T. T. N. Le and H. T. Nguyen, *Nanosized zincated hydroxyapatite as a promising heterogeneous heterogeneous photo-Fenton-like-kike catalyst for methylene blue degradation*, Advances in Materials Science and Engineering, Vol. 2017, pp. 5978149, 2019. DOI:10.1155/2019/5978149

15. H. T. Nguyen et al., *Constructing a novel Ag_2MoO_4/MIL-101(Fe)/Ag composite for efficient crystal violet degradation via heterogeneous photo-Fenton-like-like process*, Chemical Engineering Science, Vol. 284, p. 119487, 2024. DOI:10.1016/j.ces.2023.119487

16. C. Sronsri, K. U-yen and W. Sittipol, *Quantitative analysis of calcium carbonate formation in magnetized water*, Materials Chemistry and Physics, Vol. 245, pp. 122735, 2020. DOI:10.1016/j.matchemphys.2020.122735

17. Q. U. Ain, U. Rasheed, Z. Chen, R. He and Z. Tong, *Activation of Fe_3O_4 /bentonite through anchoring of highly dispersed and photo-reduced Cu ions for higher pH fenton-like degradation and effective adsorption of Congo red dye*, Journal of Industrial and Engineering Chemistry, Vol. 134, pp. 327-342, 2024. DOI:10.1016/j.jiec.2023.12.062

18. F. Peng et al., *Studies on sensing properties and mechanism of CuO nanoparticles to H_2S gas*, Nanomaterials, Vol. 10, No. 4, p. 774, 2020. DOI:10.3390/nano10040774

19. M. H. Ali, M. A. K. Azad, K. A. Khan, M. O. Rahman, U. Chakma and A. Kumer, *Analysis of crystallographic structures and properties of silver nanoparticles synthesized using PKL extract and nanoscale characterization techniques*, ACS omega, Vol. 8, pp. 28133-28142, 2023. DOI:10.1021/acsomega.3c01261

20. F. Dai, Q. Zhuang, G. Huang, H. Deng and X. Zhang, *Infrared spectrum characteristics and quantification of OH groups in coal,* ACS omega, Vol. 19, pp. 17064-17076, 2023. DOI: 10.1021/acsomega.3c01336

21. A. Dutta, *Fourier transform infrared spectroscopy* in Spectroscopic methods for nanomaterials characterization, Vol. 2, S. Thomas, R. Thomas, A. K. Zachariah, R. K. Mishra. San Diego, Elsevier, 2017, pp. 73-93.

22. Y. Zhang, W. Sun and W. Yin, *Precise regulation of UV/H_2O_2 processes: •OH generation/reaction and DOM transformation as the main free radical*

scavenger, Water Research, Vol. 277, p. 123282, 2025. DOI: 10.1016/j.watres.2025.123282

23. Z. A. Messaoudi et al., *Adsorption and photocatalytic degradation of crystal violet dye under sunlight irradiation using natural and modified clays by zinc oxide*, Chemical Methodologies, Vol. 6, pp. 661-676, 2022. DOI: 10.22034/chemm.2022.340376.1507
24. I. Creţescu, D. Lutic, *Advanced removal of crystal violet dye from aqueous solutions by photocatalysis using commercial products containing titanium dioxide*, Comptes Rendus Chimie, Vol. 25, pp. 39-50, 2022. DOI: 10.5802/crchim.150/
25. A. H. Bhat, N. A. Chopan and H. T. N. Chisti, *Enhanced photocatalytic degradation of crystal violet dye and high-performance electrochemical supercapacitor applications of hydrothermally synthesised magnetic bifunctional nanocomposite (Fe_3O_4/ZnO)*, Nanotechnology, Vol. 34, p. 495604, 2023. DOI:10.1088/1361-6528/ACF6C4
26. J. M. Sánchez-Silva et al., *Hydrothermal synthesis of a photocatalyst based on Byrsonima crassifolia and TiO_2 for degradation of crystal violet by UV and visible radiation*, Environmental Research, Vol. 231, 2023. DOI:10.1016/j.envres.2023.116280

Received: May 20, 2025
Revised: June 14, 2025
Accepted: June 28, 2025